Materialia 7 (2019) 100430

Contents lists available at ScienceDirect

Materialia

journal homepage: www.elsevier.com/locate/mtla

Full Length Article

Fracture toughness evaluation of nanostructured metals via a contactless crack opening displacement gauge

Zesheng You[a,*], Shoudao Qu[a], Shusen Luo[b], Lei Lu[b,*]

[a] Herbert Gleiter Institute of Nanoscience, School of Materials Science and Engineering, Nanjing University of Science and Technology, Nanjing 210094, China
[b] Shenyang National Laboratory for Materials Science, Institute of Metal Research, Chinese Academy of Sciences, Shenyang 110016, China

ARTICLE INFO

Keywords:
Fracture toughness
J-integral
Crack opening displacement
Nanotwins
Ultra-fined grains
Digital image correlation

ABSTRACT

Evaluation of the fracture toughness of nanostructured metals is largely limited by the incapability of current techniques to process samples sufficiently large for standard fracture tests. Here, a custom designed contactless crack opening displacement gauging system is presented for accurately measuring load-line displacement and instantaneous crack length during fracture tests with miniaturized specimens, which is in particular suitable for determining the fracture resistance of nanostructured metals. For illustrating the application of this gauge, the *J*-integral fracture resistance curves were determined for an ultrafine grained Cu processed by equal channel angular pressing and a nanotwinned Cu synthesized by electro-deposition. The ultrafine grained Cu exhibits a fracture toughness of 66 MPa $m^{1/2}$; while the fracture toughness is 39 and 55 MPa $m^{1/2}$ for the nanotwinned Cu with an average grain size of 6 and 16 μm, respectively. The underlying damage mechanisms responsible for the measured fracture toughness are discussed.

1. Introduction

Over the past three decades, the extraordinary mechanical behavior of nanostructured metallic materials with characteristic microstructural lengths falling in the nanometer scale has been extensively explored [1–3]. The nanostructured materials are much stronger than traditional coarse-grained counterparts and promising for engineering structural applications [4,5]. However, they have also been recognized to display dramatically reduced tensile ductility and fracture toughness [6,7]. A vast amount of studies have been devoted to deal with the trade-off between strength and ductility in nanostructured materials and to develop strategies to mitigate it [8–11]. On the contrary, much limited attention has been paid to their fracture properties [7,12,13], although holding sufficient damage tolerance is a critical prerequisite for the potential applications. As an estimation in the context of the Kitagawa–Takahashi diagrams [14], the transition crack size, above which the bearing stress is dependent on the embedded crack size, decreases from around 100 mm for low-strength conventional materials to only 30 μm for high-strength nanostructured materials [7]. Therefore, once with a presence of small cracks either arising from material processing or generated in services, the real bearing capacity is limited by the fracture toughness and the crack length, rather than solely by the flow strength. Therefore, accurately assessing the fracture toughness and developing toughening strategies for the high strength nanostructured materials is of enormous engineering importance for their future development.

The current lack of fracture mechanics investigations originates from the difficulty to produce bulk nanostructured samples with sufficient dimensions for standard fracture tests [7]. As a corollary, miniaturized fracture specimens were in general utilized instead. Currently, most available data were retrieved on nanostructured metals produced by severe plastic deformation (SPD). For instance, Pippan et al. have performed miniaturized compact tension (CT) fracture tests on ultra-fine grained (UFG) Cu [15], Ni [16], irons [17], and pearlitic steel [18] processed by high pressure torsion (HPT). Qin et al. [19,20] and Xiong et al. [21,22] studied the advantageous toughening effect of nanoscale deformation twins embedded in a matrix of nano-grains produced by dynamic plastic deformation (DPD).

Inspection of the available fracture toughness measurements of the nanostructured metals reveals that several critical points are still unsolved or not sufficiently noticed for quantifying the fracture toughness. First, due to the limited specimen size, the small scale yielding conditions of the linear elastic fracture mechanics (LEFM) no longer prevail [23,24]; and therefore, the elastic plastic fracture mechanics (EPFM), in terms of critical *J*-integral or critical crack tip opening displacement, should be adopted [15,17]. For the EPFM fracture tests, the load-line displacement should be accurately measured to quantify the total energy input into the tested specimen. However, this is still a grand challenge for miniaturized fracture specimens, because the commercial clip-on crack opening displacement (COD) gauge is not suitable owing to the limited crack mouth space. Second, crack tunneling is present with

* Corresponding authors.
E-mail addresses: zsyou@njust.edu.cn (Z. You), llu@imr.ac.cn (L. Lu).

https://doi.org/10.1016/j.mtla.2019.100430
Received 29 May 2019; Accepted 4 August 2019
Available online 8 August 2019

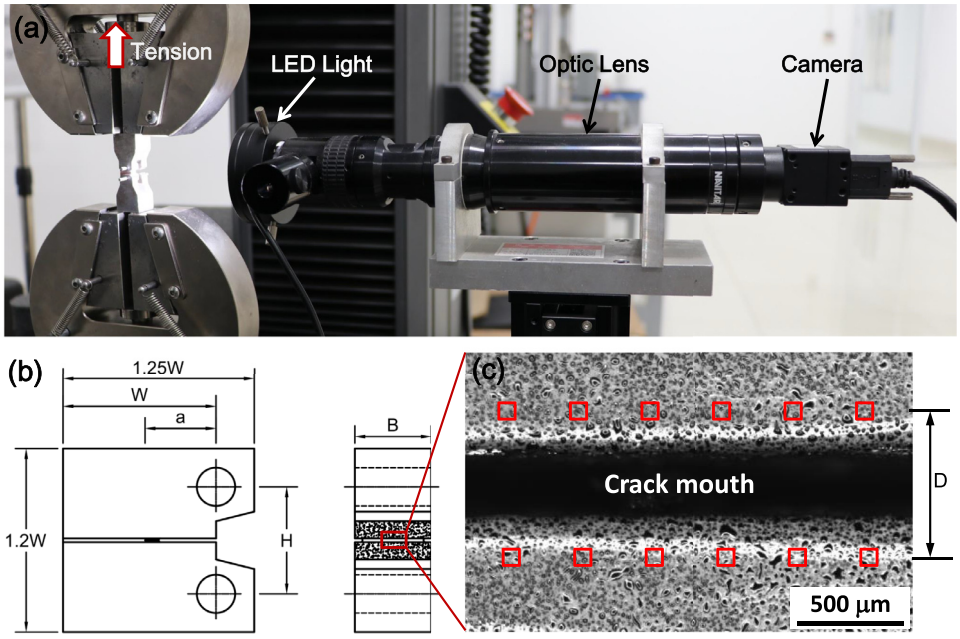

Fig. 1. (a) Contactless COD gauging system based on digital image correlation technique. (b) Schematic drawing of the CT fracture specimen. (c) Captured image of a random speckle pattern sprayed on both sides of the crack mouth, the subsets of pixels enclosed by squares are tracing markers to calculate the load-line displacement.

much more pronounced crack front extension in the center than on the surfaces of the specimen, which could exert increasingly more significant influence on the fracture resistance as the specimen size is reduced [23]. Third, the detection of crack initiation and the determination of instantaneous crack advancement also become more difficult for small specimens. Directly measuring the crack length on the surface makes little sense considering the crack tunneling effect. Finally, a complete understanding of the fracture behavior not only demands the measurement of crack initiation toughness, but also calls for knowledge on how the fracture resistance evolves with crack extension [25,26]. Currently, the valid data on the crack growth toughness is even scarcer than on the crack initiation toughness for the nanostructured materials [27].

The objective of this paper is to present a contactless COD gauging system based on digital image correlation (DIC), which solves the problems indicated above. The developed COD gauge enables precise determinations of the load-line displacement and the entire fracture resistance curve in miniaturized fracture tests. The fracture toughness of a bulk UFG Cu processed by equal channel angular pressing (ECAP) and a bulk nanotwinned (NT) Cu prepared by electro-deposition are determined by employing the COD gauge and the mechanisms responsible for the exhibited fracture resistance are discussed.

2. Methodology

2.1. Contactless COD gauge

Fig. 1(a) shows the setup of the developed contactless COD gauging system, which comprises a NAVITAR ZOOM 6000 optic lens with a work distance of ~110 mm, a SENTECH CMOS camera, a LED ring light and a computer with a custom-designed software for automatically grabbing and analyzing images. Depending on the specimen size, the magnification of the lens can be switched from 1× to 4×. The camera has a resolution of 2048 × 1088 pixels and a physical pixel size of 5.5 μm. Fig. 1(b) displays the geometry of the utilized CT fracture specimen, where W is the specimen width, and B is the specimen thickness. Two flat terraces above and below the crack mouth were purposely machined along the common plane connecting the centers of the two pin holes, which enables direct measurement of the load-line displacement without further geometry modification. Prior to the test, a random speckle pattern was generated by first painting a white background on the two terraces and then spraying random black ink spots using a medical atomizer. Fig. 1(c) displays a typical captured speckle pattern. At the start of a new test, a pattern was grabbed as reference image and several subsets of pixels (25 × 25 pixels) above and below the crack mouth were manually picked on it as tracing markers, as schematically shown in Fig. 1(c). During the test, the software continuously grabs images from the camera and computes in real-time the sub-pixel updated positions of the selected markers based on the DIC technique [28,29]. The average opening displacements of the two groups of markers with respect to their original spacing in the reference image were output as instantaneous crack mouth opening displacement (CMOD). The accuracy and resolution of the COD gauge depend on magnification of the lens, quality of the produced speckle pattern and environmental vibration. For a lens magnification of 2× used in this work, the opening displacements of a static crack without loading were recorded to scatter within a band of ±0.06 μm (namely, ±0.02 pixel) in the experimental environment. Such a small scatter can represent the good runtime accuracy of the COD gauge and must be checked before starting each test to guarantee the measurement accuracy.

2.2. Calculation of crack length

To measure crack extension during the fracture tests, the elastic compliance method involving partial unloading and reloading was employed. The crack length a at an unloading point is computed as follow [30]:

$$\frac{a}{W} = 1.000196 - 4.06319u + 11.242u^2 - 106.043u^3 + 464.335u^4 - 650.677u^5 \quad (1)$$

$$u = 1/\left(\sqrt{B_E E C^*} + 1\right) \quad (2)$$

where E is the Young's modulus, $B_E = B - (B - B_N)^2/B$ is the corresponding effective thickness, B_N is the net thickness for side-grooved specimens, and C^* is the rotation corrected elastic unloading compliance.

Fig. 2 displays the force P versus displacement v curve for an unloading segment, which as expected presents a quite good linear relationship. Through a linear regression, the elastic compliance

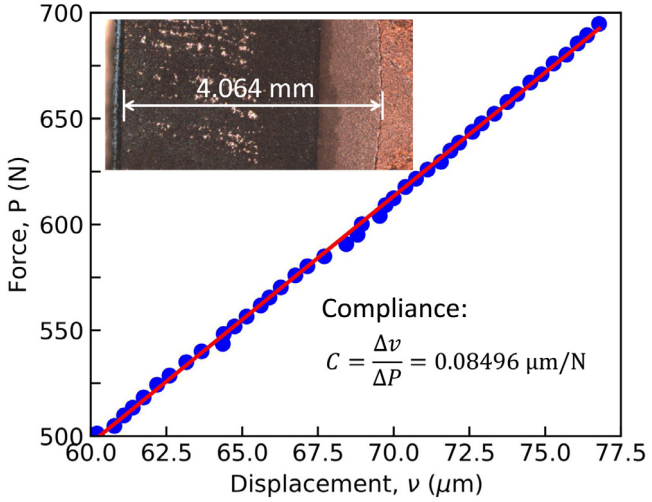

Fig. 2. Force versus load-line displacement curve for an elastic unloading stage, the inverse of its slope measures the compliance of the fracture specimen and can be used to compute the crack size. The inset in (a) displays the measurement of the corresponding crack length by an optical microscope.

$C = \Delta v/\Delta P$ is calculated as 0.08496 μm/N, and the corrected compliance C^* is 0.08380 μm/N. Using Eq. (1), the crack size is calculated to be 4.085 mm, which is in good agreement with the optic measurement (4.064 mm) shown in the inset of Fig. 2. This consistency not only demonstrates the accuracy in the measurements of load-line displacement using the developed gauging system, but also proves that the compliance method is sufficiently accurate to determine the crack extensions, which is critical for EPFM evaluation using miniaturized specimens.

2.3. Calculation of J-integral resistance curves

To construct the *J*-integral resistance *(J-R)* curve, namely, the variation of *J*-integral as a function of crack extension $\Delta a_i = a_i - a_0$ where a_0 and a_i are the initial and instantaneous crack sizes, data pairs of P_i, v_i and a_i should be recorded by conducting a series of unloading/reloading in the course of the fracture test, as schematically shown in Fig. 3(a). For each crack length a_i, the corresponding *J*-integral, J_i, can then be computed as follows [30]:

$$J_i = \frac{K_i^2(1-\nu^2)}{E} + J_i^{\mathrm{pl}} \tag{3}$$

where K_i is the stress intensity factor and calculated for a CT specimen as:

$$K_i = \frac{P_i}{(BB_N W)^{1/2}} f\left(\frac{a_i}{W}\right) \tag{4}$$

where $f(\frac{a_i}{W})$ is a geometry factor determined by the ratio of crack length a_i to the width W:

$$f\left(\frac{a_i}{W}\right) = \frac{\left(2+\frac{a_i}{W}\right)\left[0.886 + 4.64\left(\frac{a_i}{W}\right) - 13.32\left(\frac{a_i}{W}\right)^2 + 14.72\left(\frac{a_i}{W}\right)^3 - 5.6\left(\frac{a_i}{W}\right)^4\right]}{\left(1-\frac{a_i}{W}\right)^{3/2}} \tag{5}$$

For an advancing crack, the total crack growth corrected plastic *J*-integral J_i^{pl} at point *i* is recursively calculated from the following equation [30]:

$$J_i^{\mathrm{pl}} = \left(J_{i-1}^{\mathrm{pl}} + \frac{\eta_{i-1}}{b_{i-1}}\frac{A_i^{\mathrm{pl}} - A_{i-1}^{\mathrm{pl}}}{B_N}\right)\left(1 - \gamma_{i-1}\frac{a_i - a_{i-1}}{b_{i-1}}\right) \tag{6}$$

where $\eta_{i-1} = 2.0 + 0.522 b_{i-1}/W$, $\gamma_{i-1} = 1.0 + 0.76 b_{i-1}/W$ and $b_i = W - a_i$ is the uncracked ligament size. The quantity $A_i^{\mathrm{pl}} - A_{i-1}^{\mathrm{pl}}$ is the increment of the plastic work A^{pl}. As shown in Fig. 3(b), it can be approximately computed from the force versus plastic displacement $v_i^{\mathrm{pl}} = v_i - P_i C_i$ curve as:

$$A_i^{\mathrm{pl}} - A_{i-1}^{\mathrm{pl}} = \frac{(P_i + P_{i-1})\left(v_i^{\mathrm{pl}} - v_{i-1}^{\mathrm{pl}}\right)}{2} \tag{7}$$

2.4. Determination of critical fracture toughness J_{IC} and K_{IC}

Once a *J-R* curve is constructed, a provisional critical *J* integral, J_Q, is generally defined as the intersection point of the *J-R* curve with the 0.2 mm offset crack blunting line ($J = 2\sigma_Y \Delta a$, where σ_Y is the flow stress represented by the mean value of the yield strength σ_{ys} and the ultimate tensile strength σ_{uts}). The J_Q value can be regarded as a size-independent plane strain fracture toughness, J_{IC}, only when the requirements for *J*-field dominance and the plane strain conditions are satisfied, namely, $B_N, b_0 > 10 J_Q/\sigma_Y$, where b_0 is the initial uncracked ligament length [30]. The fracture toughness represented by critical stress intensity factor, K_{IC}, can then be calculated from J_{IC} by the following relationship:

$$K_{IC} = \sqrt{\frac{E J_{IC}}{1-\nu^2}} \tag{8}$$

where ν is the Possion's ratio.

3. Fracture tests

For the purpose of demonstrating the application of the contactless COD gauging system, fracture specimens with $W = 8$ mm, $B = 4$ mm and an initial notch of ~3 mm depth were machined from two different nanostructured metals by electrical discharge machining. The specimens were then fatigue pre-cracked under tension-tension mode in an Instron E3000 electro-dynamic test instrument at a frequency of 30 Hz to obtain an initial sharp crack tip. After the fatigue pre-cracking, the total initial crack size a_0 falls in the $0.45\,W < a_0 < 0.55\,W$ range. In order to suppress crack tunneling and make the crack front uniformly extend, grooves of 10%*B* deep was additionally machined on both specimen sides after fatigue pre-cracking.

The fracture tests were performed on an Instron 5982 tensile machine with a load cell of 5 kN capacity under displacement control. The loading displacement rate is about 0.25 mm min^{-1}. The forces from the tensile machine and the displacements from the COD gauge were recorded continuously at a rate of ~3 Hz through the tests. Unloading/reloading sequences were conducted at an interval of 0.05 mm with an unloading displacement of 0.1 mm min^{-1}. To ensure the reproducibility, the fracture tests were repeated at least three times for each specimen.

4. Fracture toughness of ultra-fine grained copper

The ultra-fine grained (UFG) copper was produced by equal channel angular pressing (ECAP) via route B_C, as described in detail in Ref. [31]. The ECAP treatment was repeated eight passes at a pressing speed of about 2 mm s^{-1} at room temperature. Fig. 4 illustrates the typical resulted microstructure observed in the transverse direction (TD), which is slightly inhomogeneous in terms of grain morphology. In some areas grains or subgrains are still elongated and occupied by high density of accumulated dislocations; while in other regions well-recovered equiaxed grains with fairly fewer dislocations are formed. These microstructural features are in good agreement with previous reports on the UFG Cu similarly treated [32,33]. Measurements revealed that the grain size ranges from 500 to 1000 nm with an average of ~800 nm. In this work, as an example, the fracture toughness was evaluated along the T-E orientation, namely, the crack plane is normal to the TD, while the crack propagation direction is parallel to the extrusion direction (ED).

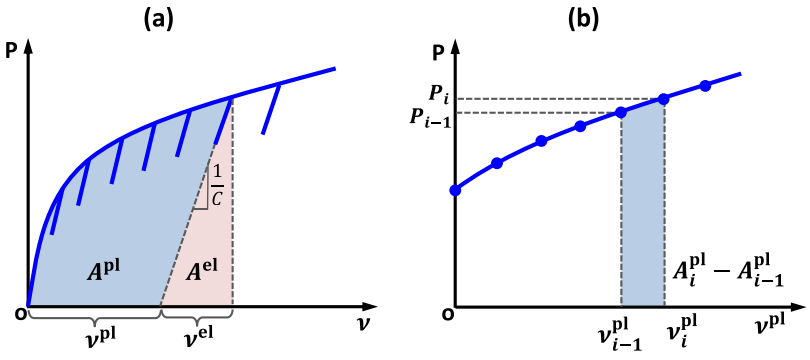

Fig. 3. Schematic representation of (a) load–displacement curve with partial unloading segments for determining the compliance C and the crack size; (b) incremental plastic area of load versus plastic displacement curve from step i-1 to i.

Table 1
Summary of the fracture experiments for the UFG Cu with the non-side-grooved (NSG) and the side-grooved (SG) specimens with $W = 4$ and 8 mm. B_N, net specimen thickness; J_Q, provisional critical J-integral; σ_Y, effective flow strength; K_{IC}, critical stress intensity factor; J_{1mm}, J-integral at a crack extension of 1 mm.

Sample	B_N (mm)	$10J_Q/\sigma_Y$ (mm)	J_Q (kJm^{-2})	K_{IC} (MPa m$^{1/2}$)	J_{1mm} (kJm^{-2})
NSG	4	2.19 ± 0.06	87 ± 2	–	222 ± 8
SG ($W = 4$ mm)	3.2	0.83 ± 0.08	33 ± 3	66 ± 3	60 ± 5
SG ($W = 8$ mm)	6.4	0.85	34	67	53

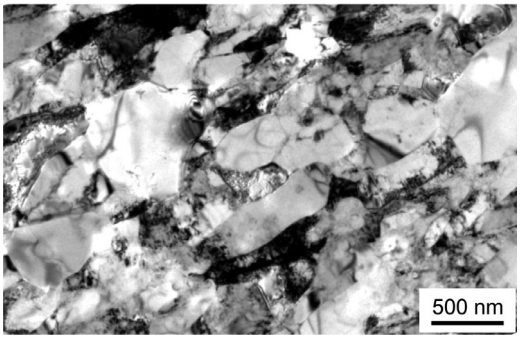

Fig. 4. TEM bright field micrograph showing the UFG microstructure in the Cu subjected to 8 passes of ECAP.

In addition, to demonstrate the strong influence of crack tunneling on the exhibited fracture resistance, fracture tests using specimens with and without side grooves were carried out and compared.

Fig. 5(a) displays the experimental force versus displacement curves, with several partial unloading segments readily visible for measuring compliances and crack extensions. The curves significantly deviate from the initial linear elastic relationship before reaching a maximum force, indicating substantial crack tip plasticity prior to crack initiation. Therefore, the LEFM method cannot be applied for the fracture toughness evaluation here. After the maximum load is reached, the non-side-grooved sample exhibits slower force reduction with loading and appears to be more stable than the side-grooved counterpart. Fig. 5(b) shows the constructed J-R curves of the UFG Cu and Table 1 summaries the obtained fracture parameters. The J-integral value for the non-side-grooved sample increases significantly from ~25 kJ m^{-2} at the onset of crack initiation to ~222 kJ m^{-2} at a crack extension of 1.0 mm. This trend is quite similar to that reported for the HPT copper with slightly smaller grains [15], which is included in Fig. 5(b) for comparison. However, this pronounced rising fracture resistance curve behavior should not be regarded as an inherent feature associated with the UFG structure. As displayed in Fig. 6(a), the crack front delineated by post fatigue is rather curved for the non-side-grooved sample. There is almost no crack advance on the specimen surfaces, whereas the crack front in the specimen center has propagated for a very long distance (~2 mm). Caused by the

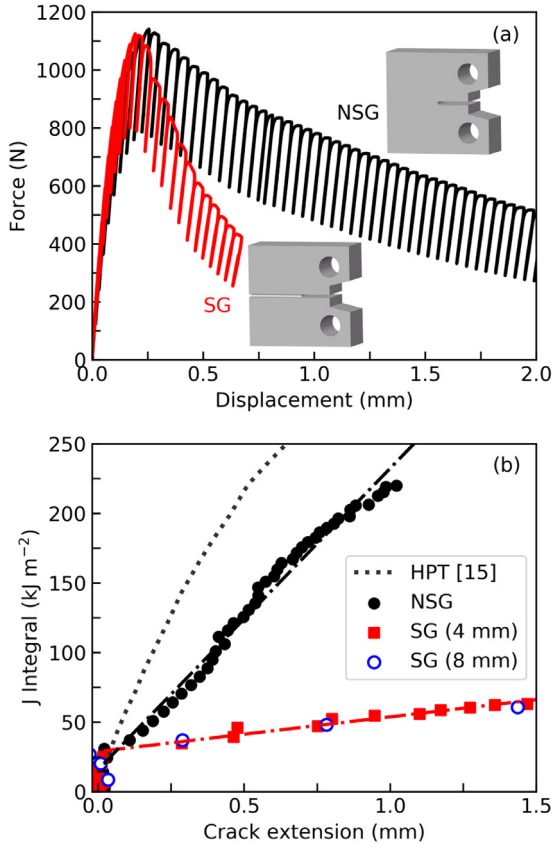

Fig. 5. (a) Force versus displacement curves for the non-side-grooved (NSG) and the side-grooved (SG) miniaturized fracture specimens of the UFG Cu; (b) corresponding J-R curves showing stable crack growth. The J-R curve for the UFG Cu processed by HPT is included for comparison [15]. To demonstrate the size independence, the J-R curves for specimens of 4 and 8 mm thickness are compared in (b).

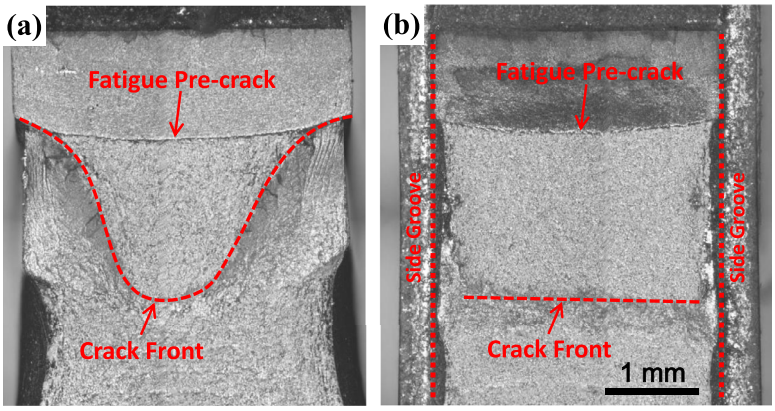

Fig. 6. Overall fracture surfaces for (a) the non-side-grooved and (b) the side-grooved specimens, a verification that the crack tunneling as shown in (a) can be suppressed by side grooving.

presence of crack tunneling, the uncracked trailing segments strongly drag the broken surfaces, leading to the observed rapid *J*-integral growing as the crack propagates.

On the contrary, for the side-grooved sample, the crack front is kept roughly straight during crack extension, see Fig. 6(b), an indication that the crack advances uniformly through the thickness. Accompanying this change is a substantial flattening of the *J*-*R* curve with crack extension, as shown in Fig. 5(b). There is only a *J*-integral increment of ~30 kJ m^{-2} as the crack extends to 1 mm. Since it was proven that the specimen size met the requirement for plane strain conditions ($B_N = 3.2$ mm > $10J_Q/\sigma_Y$, Table 1), the obtained critical fracture toughness J_{IC} (33 ± 3 kJ m^{-2}) and the corresponding K_{IC} (66 ± 3 MPa m$^{1/2}$) are size independent according to the ASTM standard [30]. This point is further verified by fracture tests using specimens of double thickness ($B = 8$ mm). As shown in Fig. 5(b), the *J*-*R* curve of the $B = 8$ mm sample overlaps with that of the $B = 4$ mm sample, an indication of the negligible effect of specimen thickness. Therefore, the obtained fracture toughness can be regarded as a valid property of the UFG Cu.

The fracture resistance of the UFG Cu is much reduced compared with the coarse grained counterpart (~200 MPa m$^{1/2}$), although still superior to many engineering Al alloys and some Ti alloys (30–50 MPa m$^{1/2}$) [34]. The reduced fracture toughness is believed to be relevant with the incorporated high density grain boundaries (GBs) [12]. The GBs and triple junctions at the sub-micron scale are considered as the primary initiation sites for micro-voids [15,35,36]. As a consequence, the void spacing is much smaller in the UFG and nanocrystalline metals than that controlled by particle spacing in conventional metals, suppressing the resistance to ductile tearing [37]. To get over this drawback, additional toughening mechanisms should be incorporated. For instance, toughening arising from crack deflection, crack delamination or crack divider has been reported to significantly increase the fracture toughness in certain orientations of UFG Ni and Fe with elongated grains [17,38]. Analogous toughening associated with substantial crack deflection in the ECAP Cu will be presented in a forthcoming paper.

5. Fracture toughness of nanotwinned copper

There have been numerous studies on nanotwinned (NT) metals with an average twin thickness less than 100 nm which offer an excellent balance of high strength, considerable tensile ductility and enhanced fatigue performance [8,9,39–42]. Nevertheless, limited attention has been paid on their fracture behavior [13,43]. Singh et al. revealed a larger fracture toughness in high density NT Cu ($K_{IC} = 17.2$ MPa m$^{1/2}$) than in low density NT Cu ($K_{IC} = 14.8$ MPa m$^{1/2}$) [44]. However, the electrodeposited samples they tested were too thin to satisfy the plane strain conditions and thus the results were thickness dependent and could not reflect the inherent fracture resistance of the NT structure.

Recently, we successfully developed a direct-current electrodeposition technique that enabled the preparation of bulk NT Cu of several millimeters thick [45]. The NT Cu consists of columnar grains with a high density of nanoscale growth twins preferentially oriented parallel to the electro-deposition plane [45,46]. As a consequence, there is a strong {1 1 1} out-of-plane fibrous texture along the deformation direction [45]. Luo et al. studied firstly the effect of specimen thickness on the fracture toughness of the NT sample [46]. The crack front line was perpendicular to the deposition plane and aligned with the fibrous texture, while the crack propagation direction is in the deposition plane, constrained by the limited thickness of the deposited samples. The results show that below a critical specimen thickness of ~1.0 mm, plane stress state prevails ahead of the crack tip and the critical *J*-integral (J_C) decreases with decreasing thickness. With increasing thickness above the critical value, J_C is reduced from a peak value of 15.6 kJ m^{-2} and settles gradually to a thickness-independent value (8.4 kJ m^{-2}) when the crack tip is primarily under plane strain state [46]. The corresponding plane strain fracture toughness K_{IC} is 33 MPa m$^{1/2}$ [46].

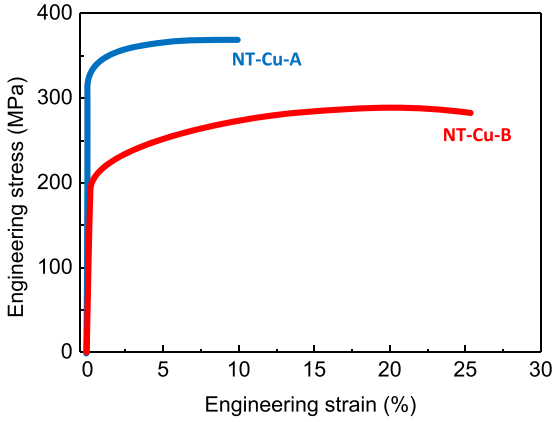

Fig. 7. Typical engineering stress–strain curves for the NT-Cu-A with an average grain size of 6 μm and the NT-Cu-B with an average grain size of 16 μm, both samples have a similar twin spacing.

In this study, in order to further unveil the grain size effect on the fracture resistance, two samples with different grain sizes and almost the same twin thickness were prepared by adjusting the electro-deposition parameters [31]. Statistics of the microstructure via scanning electron microscope (SEM) and transmission electron microscope (TEM) reveals an average grain size of 6 μm and a mean twin thickness of 51 nm for the first sample, referred to as NT-Cu-A hereafter. While for the second sample, denoted as NT-Cu-B, the average grain size and twin thickness are 16 μm and 65 nm, respectively. Most TBs are coherent and devoid of pre-existing dislocations. The microstructure of the as-deposited samples has been presented in more detail elsewhere [45]. Fig. 7 shows the corresponding engineering stress-strain curves. In good agreement with

Table 2
Microstructural parameters and mechanical properties of the columnar-grained Cu with nanoscale twins. d, average grain size; λ, average twin thickness; σ_{ys}, 0.2% offset yield strength; σ_{uts}, ultimate tensile strength; δ_u, uniform elongation; δ_f, elongation to fracture.

Sample	d (μm)	λ (nm)	σ_{ys} (MPa)	σ_{uts} (MPa)	δ_u (%)	δ_f (%)	J_{IC} (kJ m^{-2})	K_{IC} (MPa m$^{1/2}$)
NT-Cu-A	6	51	312 ± 13	366 ± 7	8.7 ± 1.6	11.2 ± 2.0	12	39
NT-Cu-B	16	65	210 ± 15	278 ± 14	20.5 ± 2.1	28.0 ± 2.8	23	55

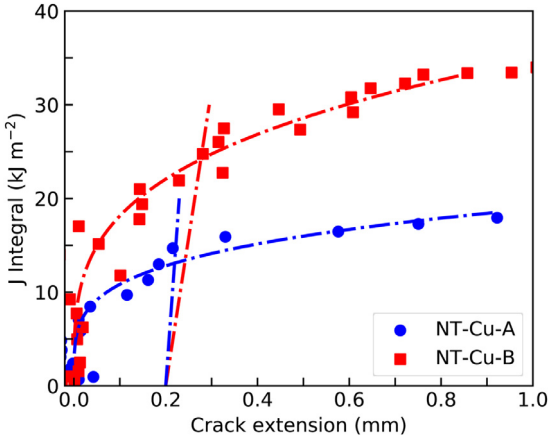

Fig. 8. Typical *J-R* curves for the NT-Cu-A with an average grain size of 6 μm and the NT-Cu-B with an average grain size of 16 μm, both samples have a similar twin spacing.

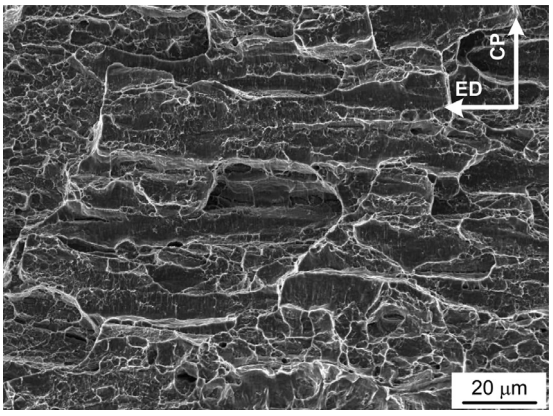

Fig. 9. Characteristic fracture surfaces of the NT-Cu-A with an average grain size of 6 μm, on which plenty of ridges and grooves can be identified along the electro-deposition direction. The crack propagation (CP) and electro-deposition (ED) directions are indicted by arrows.

Ref. [45], the yield and the tensile strengths of the NT-Cu-A with smaller grains are larger than those of the NT-Cu-B, but the uniform and the fracture elongations turn out to be smaller.

The obtained *J-R* curves for the two NT Cu samples are shown in Fig. 8. Obviously, increment in grain size enhances the resistance to fracture. For the NT-Cu-B with larger grains, the *J*-integral increases from ~15 to ~35 kJ m^{-2} as the crack stably extends to 1 mm, displaying a pronounced rising fracture resistance curve behavior; on the contrary, the *J*-integral increment is only 5 kJ m^{-2} for the NT-Cu-A (from ~10 to ~15 kJ m^{-2}). The critical fracture toughness J_{IC} of the NT-Cu-B is 23 kJ m^{-2} (K_{IC} = 55 MPa m$^{1/2}$), much larger than that for the NT-Cu-A (J_{IC} = 12 kJ m^{-2}, K_{IC} = 39 MPa m$^{1/2}$). The tensile and fracture properties are summarized in Table 2.

Fig. 9 displays the typical fracture surface morphology for the NT Cu with highly aligned TBs. There are plenty of obvious ridges and grooves aligned with the deposited columnar grains, a good reminiscence of crack growth along the GBs. As mentioned above, the crack front line is normal to the deposition plane and the TBs. Constrained by the plane strain state at the crack tip, the strain perpendicular to the TBs is negligible. As a result, the crack tip deformation should be dominantly accommodated by threading dislocations with Burgers vector parallel to TBs and moving inside the twin/matrix lamellar channels [45,46]. These threading dislocations gradually accumulate against the confronted GBs with increasing deformation, giving rise to pronounced back-stress [47] and significant local stress intensification in the vicinity of GBs [48]. Eventually, micro-voids nucleate and grow preferentially along the GBs, leading to crack extension. This failure mode is different from the in-situ TEM observations (under plane strain state) that cracks extend in an intragranular manner and interact with confronted TBs [43,49–51]. The stress state and TB orientation must strongly influence the underlying failure mechanism and the fracture resistance of the NT materials, which deserves further in-depth investigations.

The higher fracture toughness of the NT-Cu-B compared with that of the NT-Cu-A can be rationalized by several effects. First, increment in grain size enhances the strain hardening and deformation capability of the NT metals [45,52], which is beneficial to improve the crack tip plasticity. Second, the density of crack nucleation sites along the GBs is reduced for coarser grains. Third, larger grains make crack propagation path more tortuous, which consumes more irreversible energy to extend the crack front.

6. Summary and perspective

The developed contactless COD gauging system has been proven to accurately measure the load-line displacements of miniaturized fracture specimens and thus to enable the crack size determination via elastic compliance method, which is particularly advantageous for the fracture toughness evaluations of the nanostructured metals of limited sample volume. Provided that the requirements of straight crack-front line, *J*-field dominance and plane strain state are all satisfied, the obtained fracture toughness values are size-independent and comparable among diverse materials or different microstructures. This feature is of special scientific and engineering importance for microstructural design targeting for optimizing the balance between fracture toughness and strength.

The COD gauge has been utilized to evaluate the fracture resistance of the ECAP UFG Cu and the electrodeposited columnar-grained NT Cu in this study, and of DPD NT Cu [23] and NT 316 L stainless steel [24] previously as well. The UFG Cu with a mean grain size of ~800 nm exhibits a critical fracture toughness K_{IC} of 66 ± 3 MPa m$^{1/2}$ in the T-E cracking orientation and diminishing fracture resistance curve behavior. The reduced fracture resistance is in general proposed to result from the high density GBs that provide nucleation sites and shorten spacing of micro-voids. The fracture toughness of the NT Cu is elevated from 39 to 55 MPa m$^{1/2}$ with increasing grain size from 16 to 65 μm while almost keeping the same twin thickness. Because the crack front line is aligned with the columnar grains and the TB normal, the plane strain constraint leads to threading dislocation accumulation along GBs and micro-void nucleation and growth therein. Coarser grains enhance plasticity, reduce micro-void nucleation sites, and promote crack path tortuosity, all positively contribute to the fracture resistance.

Currently, compared with the large amount of diverse nanostructured materials emerging over the past years, the available fracture toughness data are still far too scarce to establish a consolidated relationship between the various nanostructures and their inherent sensitivities to crack-like defects. Fairly more experimental data remain to be accumulated to clearly elucidate the influences of microstructural parameters such as grain size/twin thickness/lamellar spacing, grain morphologies, crystallographic texture, GB characteristics, chemical impurities, volume fraction and spatial distribution of precipitates or second-phase inclusions, etc. The thermal and mechanical microstructural stabilities should also be noticed because the microstructural evolution could interact or compete with void nucleation and growth processes and make them behave rather differently from those in the microstructure stable metals.

In addition, there has been a growing interest in recent years in heterogeneous and gradient nanostructures, where spatially varying microstructures were introduced to promote strain hardening [11,42,53–55]. It has been demonstrated that the synergy of strength and tensile ductility can be enhanced via optimized architectural tailoring and hence is advantageous for the structural applications. However, the investigations on the fracture properties of these unique nanostructured metals are still lacking. For instance, it should be clarified beforehand whether the purposely incorporated boundaries between the hard and soft domains are also beneficial to the fracture resistance, or they conversely act as stress raisers and promote damage development. The established valid EPFM experiment based on the *J*-integral, as presented here, offers many opportunities for improving the fundamental understanding of how the damage/failure process associated with the various nanostructures influences the macroscopic fracture toughness.

Acknowledgments

The authors acknowledge financial support from the National Key R&D Program of China (Grant no. 2017YFA0204403) and the Natural Science Foundation of Jiangsu Province, China (Grant no. BK20161498). LL acknowledges financial support by National Science Foundation of China (Grant numbers 51420105001, 51471172, 51601196 and U1608257) and the Key Research Program of Frontier Science, CAS. SQ acknowledges the Postgraduate Research & Practice Innovation Program of Jiangsu Province (Grant no. KYCX180408). ZY would like to thank Prof. J.T. Wang for providing the ECAP Cu samples.

Declaration of Competing Interest

The authors declare that they have no known competing financial interests or personal relationships that could have appeared to influence the work reported in this paper.

References

[1] K. Lu, Stabilizing nanostructures in metals using grain and twin boundary architectures, Nat. Rev. Mater. 1 (2016) 16019.
[2] I.A. Ovid'ko, R.Z. Valiev, Y.T. Zhu, Review on superior strength and enhanced ductility of metallic nanomaterials, Prog. Mater. Sci. 94 (2018) 462–540.
[3] M.A. Meyers, A. Mishra, D.J. Benson, Mechanical properties of nanocrystalline materials, Prog. Mater. Sci. 51 (2006) 427–556.
[4] R.Z. Valiev, T.G. Langdon, Principles of equal-channel angular pressing as a processing tool for grain refinement, Prog. Mater. Sci. 51 (2006) 881–981.
[5] R.Z. Valiev, R.K. Islamgaliev, I.V. Alexandrov, Bulk nanostructured materials from severe plastic deformation, Prog. Mater. Sci. 45 (2000) 103–189.
[6] Y. Zhu, X. Liao, Nanostructured metals: retaining ductility, Nat. Mater. 3 (2004) 351–352.
[7] R. Pippan, A. Hohenwarter, The importance of fracture toughness in ultrafine and nanocrystalline bulk materials, Mater. Res. Lett. 4 (2016) 127–136.
[8] K. Lu, L. Lu, S. Suresh, Strengthening materials by engineering coherent internal boundaries at the nanoscale, Science 324 (2009) 349–352.
[9] L. Lu, X. Chen, X. Huang, K. Lu, Revealing the maximum strength in nanotwinned copper, Science 323 (2009) 607–610.
[10] X. Wu, P. Jiang, L. Chen, F. Yuan, Y.T. Zhu, Extraordinary strain hardening by gradient structure, Proc. Natl. Acad. Sci. USA 111 (2014) 7197–7201.
[11] T.H. Fang, W.L. Li, N.R. Tao, K. Lu, Revealing extraordinary intrinsic tensile plasticity in gradient nano-grained copper, Science 331 (2011) 1587–1590.
[12] A. Pineau, A. Amine Benzerga, T. Pardoen, Failure of metals III: fracture and fatigue of nanostructured metallic materials, Acta Mater 107 (2016) 508–544.
[13] Z. You, L. Lu, Deformation and fracture mechanisms of nanotwinned metals, Natl. Sci. Rev. 4 (2017) 519–520.
[14] H. Kitagawa, S. Takahashi, Applicability of fracture mechanics to very small cracks or the cracks in the early stage, in: Proceedings of the Second International Conference on Mechanical Behavior of Materials, Metals Park, OH, American Society for Metals, 1976, pp. 627–631.
[15] A. Hohenwarter, R. Pippan, A comprehensive study on the damage tolerance of ultrafine-grained copper, Mater. Sci. Eng. A 540 (2012) 89–96.
[16] G.B. Rathmayr, R. Pippan, Extrinsic and intrinsic fracture behavior of high pressure torsion deformed nickel, Scr. Mater. 66 (2012) 507–510.
[17] A. Hohenwarter, R. Pippan, Fracture of ECAP-deformed iron and the role of extrinsic toughening mechanisms, Acta Mater. 61 (2013) 2973–2983.
[18] C. Kammerhofer, A. Hohenwarter, S. Scheriau, H.P. Brantner, R. Pippan, Influence of morphology and structural size on the fracture behavior of a nanostructured pearlitic steel, Mater. Sci. Eng. A 585 (2013) 190–196.
[19] E.W. Qin, L. Lu, N.R. Tao, J. Tan, K. Lu, Enhanced fracture toughness and strength in bulk nanocrystalline Cu with nanoscale twin bundles, Acta Mater. 57 (2009) 6215–6225.
[20] E.W. Qin, L. Lu, N.R. Tao, K. Lu, Enhanced fracture toughness of bulk nanocrystalline Cu with embedded nanoscale twins, Scr. Mater. 60 (2009) 539–542.
[21] L. Xiong, Z.S. You, L. Lu, Fracture behavior of an austenitic stainless steel with nanoscale deformation twins, Scr. Mater. 127 (2017) 173–177.
[22] L. Xiong, Z.S. You, L. Lu, Enhancing fracture toughness of nanotwinned austenitic steel by thermal annealing, Scr. Mater. 119 (2016) 55–59.
[23] S.S. Luo, Z.S. You, L. Lu, Intrinsic fracture toughness of bulk nanostructured Cu with nanoscale deformation twins, Scr. Mater. 133 (2017) 1–4.
[24] L. Xiong, Z.S. You, S.D. Qu, L. Lu, Fracture behavior of heterogeneous nanostructured 316L austenitic stainless steel with nanotwin bundles, Acta Mater. 150 (2018) 130–138.
[25] R.O. Ritchie, A.W. Thompson, On macroscopic and microscopic analyses for crack initiation and crack growth toughness in ductile alloys, Metall. Trans. A 16 (1985) 233–248.
[26] S. Suresh, A.K. Vasudevan, On the relationship between crack initiation toughness and crack growth toughness, Mater. Sci. Eng. 79 (1986) 183–190.
[27] A. Hohenwarter, R. Pippan, Fracture and fracture toughness of nanopolycrystalline metals produced by severe plastic deformation, Phil. Trans. R. Soc. A 373 (2015) 20140366.
[28] M.A. Sutton, J.-J. Orteu, H.W. Schreier, Image Correlation for Shape, Motion and Deformation Measurements: Basic Concepts, Theory and Applications, Springer, New York, 2009.
[29] B. Pan, K. Qian, H. Xie, A. Asundi, Two-dimensional digital image correlation for in-plane displacement and strain measurement: a review, Meas. Sci. Technol. 20 (2009) 062001.
[30] ASTM E1820-15, Standard Test Method for Measurement of Fracture Toughness, American Society of Testing and Materials, PhiladelphiaPA, 2015.
[31] Y. Jiang, R. Zhu, J.T. Wang, Z.S. You, An investigation on rolling texture transition in copper preprocessed by equal channel angular pressing, J. Mater. Sci. 51 (2016) 5609–5624.
[32] F. Dalla Torre, A. Gazder, E. Pereloma, C. Davies, Recent progress on the study of the microstructure and mechanical properties of ECAE copper, J. Mater. Sci. 42 (2007) 1622–1637.
[33] F. Dalla Torre, R. Lapovok, J. Sandlin, P.F. Thomson, C.H.J. Davies, E.V. Pereloma, Microstructures and properties of copper processed by equal channel angular extrusion for 1-16 passes, Acta Mater. 52 (2004) 4819–4832.
[34] J.G. Kaufman, R.L. Moore, P.E. Schilling, Fracture toughness of structural aluminum alloys, Eng. Fract. Mech. 2 (1971) 197–210.
[35] K.S. Kumar, H. Van Swygenhoven, S. Suresh, Mechanical behavior of nanocrystalline metals and alloys, Acta Mater. 51 (2003) 5743–5774.
[36] J.A. Sharon, H.A.I. Padilla, B.L. Boyce, Interpreting the ductility of nanocrystalline metals, J. Mater. Res. 28 (2013) 1539–1552.
[37] T. Pardoen, J.W. Hutchinson, Micromechanics-based model for trends in toughness of ductile metals, Acta Mater. 51 (2003) 133–148.
[38] A. Hohenwarter, R. Pippan, Fracture toughness evaluation of ultrafine-grained nickel, Scr. Mater. 64 (2011) 982–985.
[39] Q. Pan, H. Zhou, Q. Lu, H. Gao, L. Lu, History-independent cyclic response of nanotwinned metals, Nature 551 (2017) 214–217.
[40] Y.F. Shen, L. Lu, Q.H. Lu, Z.H. Jin, K. Lu, Tensile properties of copper with nano-scale twins, Scr. Mater. 52 (2005) 989–994.
[41] Q.S. Pan, L. Lu, Strain-controlled cyclic stability and properties of Cu with highly oriented nanoscale twins, Acta Mater. 81 (2014) 248–257.
[42] Z. Cheng, H. Zhou, Q. Lu, H. Gao, L. Lu, Extra strengthening and work hardening in gradient nanotwinned metals, Science 362 (2018) 559.
[43] Z. Zeng, X. Li, L. Lu, T. Zhu, Fracture in a thin film of nanotwinned copper, Acta Mater. 98 (2015) 313–317.
[44] A. Singh, L. Tang, M. Dao, L. Lu, S. Suresh, Fracture toughness and fatigue crack growth characteristics of nanotwinned copper, Acta Mater. 59 (2011) 2437–2446.
[45] Z.S. You, L. Lu, K. Lu, Tensile behavior of columnar grained Cu with preferentially oriented nanoscale twins, Acta Mater. 59 (2011) 6927–6937.
[46] S. Luo, Z. You, L. Lu, Thickness effect on fracture behavior of columnar-grained Cu with preferentially oriented nanoscale twins, J. Mater. Res. 32 (2017) 4554–4562.
[47] H. Wang, Z. You, L. Lu, Kinematic and isotropic strain hardening in copper with highly aligned nanoscale twins, Mater. Res. Lett. 6 (2018) 333–338.

[48] Z. You, L. Lu, Effect of strain rate on tensile ductility and fracture behavior of bulk nanotwinned copper, Adv. Eng. Mater. 17 (2015) 1754–1759.
[49] Z.W. Shan, L. Lu, A.M. Minor, E.A. Stach, S.X. Mao, The effect of twin plane spacing on the deformation of copper containing a high density of growth twins, JOM 60 (2008) 71–74.
[50] S.-W. Kim, X. Li, H. Gao, S. Kumar, In situ observations of crack arrest and bridging by nanoscale twins in copper thin films, Acta Mater. 60 (2012) 2959–2972.
[51] Y.A. Shin, S. Yin, X. Li, S. Lee, S. Moon, J. Jeong, M. Kwon, S.J. Yoo, Y.-M. Kim, T. Zhang, H. Gao, S.H. Oh, Nanotwin-governed toughening mechanism in hierarchically structured biological materials, Nat. Commun. 7 (2016) 10772.
[52] X.H. Chen, L. Lu, Work hardening of ultrafine-grained copper with nanoscale twins, Scr. Mater. 57 (2007) 133–136.
[53] C.X. Huang, Y.F. Wang, X.L. Ma, S. Yin, H.W. Höppel, M. Göken, X.L. Wu, H.J. Gao, Y.T. Zhu, Interface affected zone for optimal strength and ductility in heterogeneous laminate, Mater. Today 21 (2018) 713–719.
[54] E. Ma, T. Zhu, Towards strength–ductility synergy through the design of heterogeneous nanostructures in metals, Mater. Today 20 (2017) 323–331.
[55] X. Wu, Y. Zhu, Heterogeneous materials: a new class of materials with unprecedented mechanical properties, Mater. Res. Lett. 5 (2017) 527–532.